

# Realisation of Protected Cat Qutrit via Engineered Quantum Tunnelling

Sangil Kwon,<sup>1,2,\*</sup> Daisuke Hoshi,<sup>3,4</sup> Toshiaki Nagase,<sup>3,4</sup> Daichi Sugiyama,<sup>3,4</sup> Hiroto Mukai,<sup>5,4,2</sup> Kengo Takemura,<sup>3,4</sup> Rintaro Kojima,<sup>3,4</sup> Yu Zhou,<sup>4</sup> Shohei Watabe,<sup>6,2</sup> Fumiki Yoshihara,<sup>3,2</sup> and Jaw-Shen Tsai<sup>2,7,4</sup>

<sup>1</sup>*Department of Physics and Chemistry, Daegu Gyeongbuk Institute of Science and Technology (DGIST), Dalseong-gun, Daegu, 42988, South Korea*

<sup>2</sup>*Research Institute for Science and Technology, Tokyo University of Science, Shinjuku-ku, Tokyo, 162-8601, Japan*

<sup>3</sup>*Department of Physics, Graduate School of Science, Tokyo University of Science, Shinjuku-ku, Tokyo, 162-8601, Japan*

<sup>4</sup>*RIKEN Center for Quantum Computing (RQC), Wako-shi, Saitama, 351-0198, Japan*

<sup>5</sup>*Department of Applied Physics, School of Engineering, The University of Tokyo, Bunkyo-ku, Tokyo, 113-8656, Japan*

<sup>6</sup>*College of Engineering, Shibaura Institute of Technology, Koto-ku, Tokyo, 135-8548, Japan*

<sup>7</sup>*Graduate School of Science, Tokyo University of Science, Shinjuku-ku, Tokyo, 162-8601, Japan*

(Dated: January 27, 2026)

Engineering quantum tunnelling in phase space has emerged as a viable method for creating a protected qubit with biased-noise properties. A promising approach is to combine a Kerr nonlinearity with multi-photon transitions, resulting in a system known as a Kerr parametric oscillator (KPO). In this work, we implement a three-photon KPO and explore its potential as a protected qutrit. We confirm quantum coherence by demonstrating three-photon Rabi oscillations and performing direct Wigner function measurements that reveal three-component cat-like states. We observe breathing-like dynamics in phase space, arising from exotic temporal interference between the qutrit and excited states. The frequency of this interference corresponds to the energy gap between the qutrit and excited manifolds, thereby providing an experimental hallmark of qutrit space protection. We also identify a higher-order pump term as the main mechanism suppressing photon occupation; mitigating this term is necessary to maximize protection. Our findings elucidate the basic quantum properties of the three-photon KPO and establish the first step toward its use as an alternative qutrit platform.

## I. INTRODUCTION

Fault-tolerant quantum computing requires a platform where quantum information can be easily encoded and controlled while simultaneously robustly protected from various noise sources. While superconducting circuits have emerged as a leading platform for quantum computation [1–4], their inherent susceptibility to noise, such as single-photon loss or dephasing, limits their path to full fault tolerance. Quantum error correction (QEC) is expected to form the foundation of fault-tolerant quantum computing by resolving these issues; however, the immense number of physical qubits required to construct even a single error-free logical qubit remains a significant barrier.

Bosonic codes address this challenge by leveraging the large Hilbert space of a resonator to encode a logical qubit into special quantum states [5–8]. These states are engineered to be correctable up to a certain error level, or at least robust against specific noise channels. Nevertheless, such states are only a subset of the many states realisable in the resonator, making them highly susceptible to noise that can cause the state to leak out of the computational subspace. Thus, the logical qubit states need to be preserved against various noise sources.

A notable strategy to resolve this issue is to implement a system where the logical qubit space is

composed of eigenstates. Kerr parametric oscillators (KPOs), which synergise quantum tunnelling by combining a Kerr nonlinearity and multi-photon transitions [9–11], are particularly well-suited for this approach. In a two-photon KPO, even and odd cat states serve as the eigenstates that span the logical qubit space [12, 13]. This manifold is protected against single-photon loss and low-frequency dephasing by an energy gap that separates the qubit space from non-computational space. In this sense, we call KPO cat states as protected qubit space. Moreover, by using the two opposite coherent states as the computational basis, the two-photon KPO offers the biased-noise property, in which bit-flip errors originating from single-photon loss are much less common compared to phase-flip errors [14–19]. These properties are expected to reduce the resource requirements for quantum error correction [20].

Another strategy for reducing the hardware overhead is to use qudits [21–24]. Within superconducting platforms, most qudit implementations have relied on the energy levels of anharmonic oscillators, such as transmons [25–34]. However, these multi-level systems suffer from inherent transition asymmetries; for instance, the  $|0\rangle \rightarrow |2\rangle$  transition in a transmon is dipolarly forbidden, complicating universal control. Meanwhile, the implementation of qudits within the bosonic coding framework remains relatively unexplored (Ref. [35] being a notable exception). While multi-component cat states offer a high-dimensional alternative [36, 37], they are generally not protected

---

\* email: kwon2866@gmail.com

against noise. Furthermore, performing gate operations on such states is non-intuitive and requires more control overhead compared to multi-level systems.

Building on this research direction, the implementation of protected multi-component cat states offers potential for reducing the resource required for quantum error correction. A superconducting KPO provides an ideal platform for this approach; for instance, three-component cat states can be prepared by engineering quantum tunneling using modest Kerr nonlinearity and three-photon down-conversion [38–43]. The symmetry of the states is enforced by the Hamiltonian itself, providing a more robust and controllable platform for high-dimensional quantum logic. Previous demonstrations of the three-photon KPO operated in the semiclassical regime, and thus observed neither quantum coherence nor dynamics [44, 45], despite many interesting theoretical studies and proposals associated with its quantum nature being published recently [46–55].

In this work, we experimentally realize a three-photon KPO and demonstrate that the resulting quantum states constitute a protected qutrit manifold. We first observe clear signatures of quantum coherence in the three-photon KPO, including three-photon Rabi oscillations and the characteristic inter-

ference pattern with three-fold symmetry (i.e., three-component cat-like states) in the measured Wigner functions. Next, we investigate the quantum dynamics and relaxation of the prepared states, showing that the qutrit space is protected by an energy gap. The size of this gap is measured via temporal interference between states inside and outside the qutrit space. Finally, we identify the influence of higher-order pump terms as the primary physical mechanism suppressing the size of the KPO states compared to the ideal model's expectation.

## II. RESULTS

### A. Setup

The chip employed in this work is depicted in Fig. 1a. Our KPO design for this work (Fig. 1b) was inspired by the recent work of NEC [56]. A key distinction between the KPO in this work and our previous designs [12, 13] is the reduction in the number of direct-current superconducting quantum interference devices (DC SQUIDs), thereby minimizing the flux modulation inhomogeneity.

The Hamiltonian of our system can be described as (see Sec. IV for the derivation)

$$\hat{\mathcal{H}}(t) = \Delta(t) \hat{a}^\dagger \hat{a} - \frac{K}{2} \hat{a}^\dagger \hat{a}^\dagger \hat{a} \hat{a} + \frac{P(t)}{2} [(\hat{a}^\dagger \hat{a}^\dagger \hat{a}^\dagger + \hat{a} \hat{a} \hat{a}) + \eta (\hat{a}^\dagger \hat{a}^\dagger \hat{a}^\dagger \hat{a}^\dagger \hat{a} + \hat{a}^\dagger \hat{a} \hat{a} \hat{a} \hat{a})]. \quad (1)$$

Here, we are working in units where  $\hbar = 1$ ;  $\hat{a}$  and  $\hat{a}^\dagger$  are the ladder operators for the KPO;  $\Delta (\equiv \omega_K - \omega_p/3)$  is the KPO-pump frequency detuning, where  $\omega_K$  is the transition frequency between the  $|0\rangle$  and  $|1\rangle$  states, and  $\omega_p$  is the frequency of the three-photon pump;  $K$  is the self-Kerr coefficient;  $P$  is the amplitude of the pump; and  $\eta$  is the fractional strength of the higher-order pump term. The Hamiltonian in Eq. (1) is in the rotating frame defined by  $\hat{\mathcal{H}}_0 = (\omega_p/3)\hat{a}^\dagger \hat{a}$ .

The classical version of the Hamiltonian exhibits three energy minima in phase space as shown in Fig. 1c. This classical Hamiltonian can be obtained by substituting  $\hat{a}$  and  $\hat{a}^\dagger$  in Eq. (1) with the complex variables  $\alpha$  and  $\alpha^*$ , respectively:

$$\begin{aligned} \frac{\mathcal{H}}{K} &= \frac{\Delta}{K} (x^2 + y^2) - \frac{1}{2} (x^2 + y^2)^2 \\ &\quad + \frac{P}{K} [(x^3 - 3xy^2) + \eta(x^5 - 2x^3y^2 - 3xy^4)], \end{aligned} \quad (2)$$

where  $x \equiv \text{Re}(\alpha)$  and  $y \equiv \text{Im}(\alpha)$ .

The consequence of this three-fold symmetry is that the eigenstates of a three-photon KPO is three-component cat-like states, as shown in Fig. 1d. In this work, the three nearly degenerated eigenstates closest to the energy minima form the qutrit space,  $|0_C\rangle$ ,  $|1_C\rangle$ , and  $|2_C\rangle$ , which are distinguished by the remain-

der of their photon numbers modulo 3 (Fig. 1e). For example, in the  $|0_C\rangle$  state, only Fock states with a photon number of  $3n$  (where  $n$  is an integer) are occupied. Similarly, the excited state  $|0_C^{\text{ex}}\rangle$  (the final plot in Fig. 1d) also only occupies Fock states with  $3n$  photons, like  $|0_C\rangle$ .

Throughout this work, the  $P/K$  ratio is set to 0.822. At this operating condition, the Kerr coefficient is determined to be  $K/2\pi = 1.46$  MHz. For reference, at zero pump amplitude,  $\omega_K/2\pi = 3.112$  GHz and  $K/2\pi = 1.70$  MHz. These parameters were extracted from Rabi oscillation measurements that are explained in Sec. II B. A more complete list of system parameters is presented in Table I.

### B. Three-photon Rabi oscillations

The validity of Eq. (1) is confirmed by measuring Rabi oscillations in the population of the KPO  $|0\rangle$  state, following the methodology detailed in Ref. [12]. The transmon exhibits photon number splitting once the KPO is excited, owing to the dispersive interaction between the two components. By setting the frequency of the transmon  $\pi$ -pulse to match the transmon peak corresponding to the KPO  $|0\rangle$  state, we

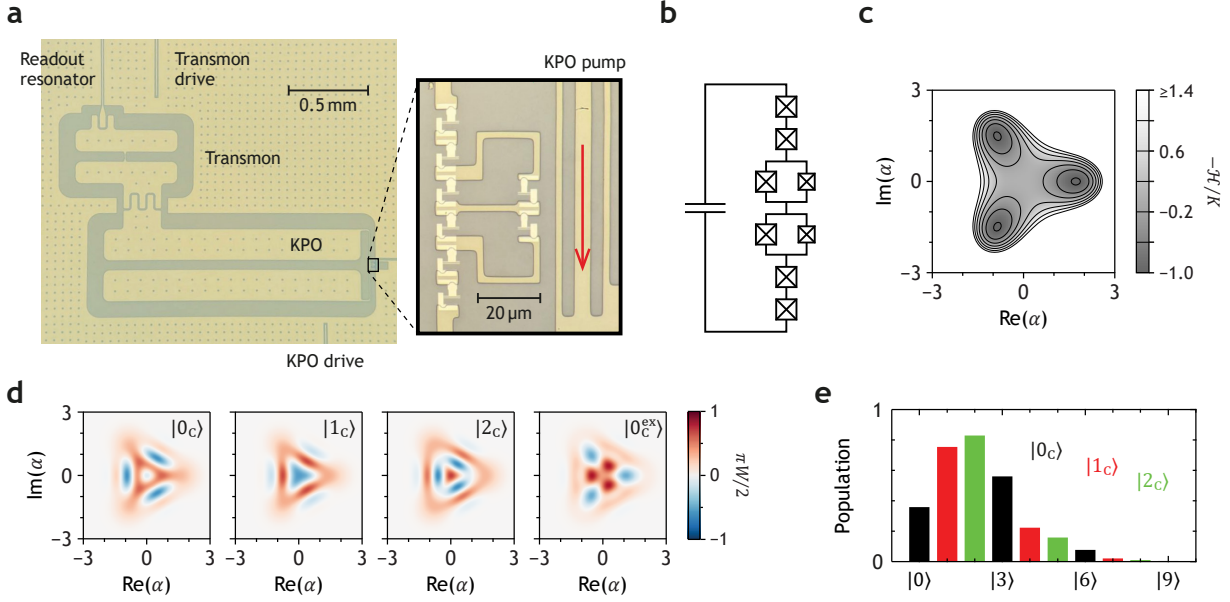


**Fig. 1: Chip and qutrit states.** **a** Photograph of the chip containing the KPO. The state of the KPO is measured by a nearby transmon and its readout resonator. **b** Circuit diagram of the Kerr parametric oscillator (KPO), which consists of two direct-current superconducting quantum interference devices (DC SQUIDS) and four junctions with a shunting capacitor. **c** The classical energy landscape corresponding to the Hamiltonian in Eq. (2). **d,e** Wigner function and the occupation probability in the Fock basis of the eigenstates of the Hamiltonian in Eq. (1). The states  $|0_c\rangle$ ,  $|1_c\rangle$ , and  $|2_c\rangle$  form the qutrit space;  $|0_c^{ex}\rangle$  is an excited state that is energetically closest to the qutrit space. For (c)–(e), the parameters are  $P/K = 0.822$ ,  $\Delta/K = 0.66$ , and  $\eta = -0.04$ .

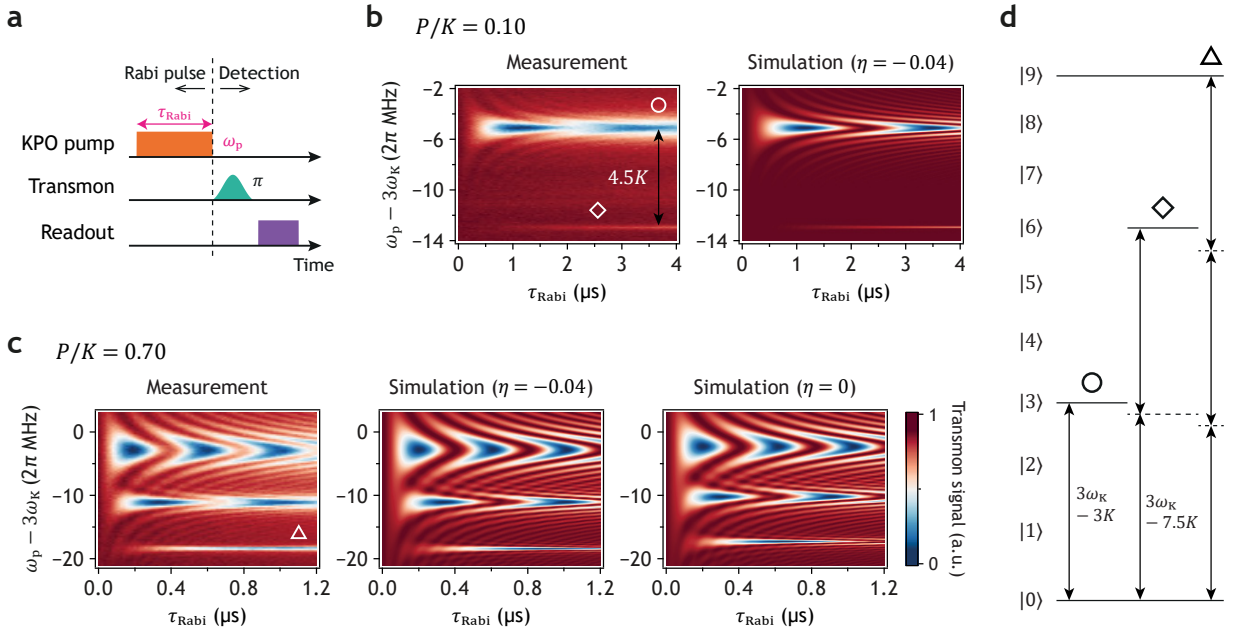


**Fig. 2: Three-photon Rabi oscillations.** **a** Pulse sequence used for measuring Rabi oscillations. The control parameters are shown in magenta, and “ $\pi$ ” denotes the transmon  $\pi$ -pulses. **b,c** Rabi oscillations observed in the weak ( $P \ll K$ ) and moderate ( $P \sim K$ ) pump regimes, respectively. The simulation results in (c) clearly show that the contribution of the higher-order pump term ( $\eta$  term) must be included to quantitatively understand the Rabi oscillations. Without  $\eta$ , the period of the higher-order signal (e.g., near  $-10$  MHz) does not match well with the experimental data. The colour in both panels represents the population of the KPO’s  $|0\rangle$  state as detected by the transmon. **d** Energy level diagram of the KPO. The symbols indicate the correspondence between the transitions and the observed signals.

can measure the population of this specific state. The overall pulse sequence is shown in Fig. 2a.

Clear Rabi oscillations are observed at the pump frequency near  $3\omega_K$ , as shown in Fig. 2b and c. The dynamics of the KPO are primarily governed by the ratio  $P/K$ . In the weak pump regime ( $P/K \ll 1$ ), two distinct signals are observed (Fig. 2b). The Rabi oscillation denoted by the circle is induced by the transition between the  $|0\rangle$  and  $|3\rangle$  states (Fig. 2d) via a four-wave mixing process. The weak signal, denoted by the diamond, originates from the transition between the  $|0\rangle$  and  $|6\rangle$  states via an eight-wave mixing process. The frequency separation between these two signals is  $4.5K$  because, in a Kerr nonlinear resonator, the energy spacing between  $|n\rangle$  and  $|n+1\rangle$  states is given by  $\omega_K - nK$ . As we increase  $P$ , the Rabi oscillation pattern becomes more complicated, and more higher-order transitions are involved. The signal denoted by the triangle in Fig. 2c, for example, roughly corresponds to the transition between the  $|0\rangle$  and  $|9\rangle$  states (Fig. 2d). All data presented in Fig. 2b and c show excellent agreement with the simulation results, thus validating the use of Eq. (1) as the model for our KPO. (For all simulations in this work, QuTiP was used [57].)

The value of  $\eta$  from the fitting is  $-0.04 \pm 0.006$  (where the error represents the standard deviation across data sets with different  $P$  values), which is significantly larger than the theoretical value of approximately  $-0.001$  [from Eq. (5)]. The fitted  $\eta$  value is mainly constrained by higher-order transitions, such as the signal near  $(\omega_p - 3\omega_K)/2\pi = -10$  MHz in Fig. 2c. Up to  $P/K = 1.0$ ,  $\eta$  does not show systematic dependence on the pump amplitude, suggesting that the large discrepancy is not induced by the pump. The reason for such a large fitted  $\eta$  is unclear; we may need to consider the influence of individual junction degrees of freedom, as our calculation of  $\eta$  assumed a single degree of freedom (see Sec. IV).

### C. Quantum coherence in Wigner functions

We access the  $|0_C\rangle$  state by ramping up the pump pulse with a  $\sin^2(\pi t/2\tau_{\text{ramp}})$  profile, following the methodology presented in Refs. [12, 13]. The resulting state of the KPO is then characterized by measuring its Wigner function via parity measurement [58, 59]. The pulse sequence for this process is shown in Fig. 3a. Although this ramping was intended to induce an adiabatic transition, a small amount of unwanted excitation is observed. The consequences of this excitation is discussed in Sec. IID.

The Wigner functions of our three-photon KPO states exhibit two essential features (Fig. 3b). Firstly, all data show triangular symmetry, which indicates the three-photon nature of our pump. Secondly, the interference-like pattern—a clear signature of quantum coherence—appears and becomes more evident as the pump detuning ( $\Delta$ ) increases, confirming that the quantum state of our KPO is a three-component

cat-like state.

The fidelity between the reconstructed and simulated density matrices is reasonably good, consistently  $\gtrsim 0.9$  (see the caption of Fig. 3b). Here, the reconstructed density matrices of the KPO were obtained via quantum state tomography with conditional generative adversarial network (QST-CGAN) [60, 61], followed by the correction of unwanted Kerr evolution during the parity measurement process [12].

To compare our measured Wigner function with simulation, we must account for the effect of single-photon loss during the parity measurement. This is because the parity measurement time ( $\approx 0.67$   $\mu$ s) is not negligible compared to the  $T_1$  of our KPO ( $\approx 4.5$   $\mu$ s). We found that the Wigner functions calculated using an effective  $T_1$  ( $T_{\text{leff}}$ ) that is twice the KPO's actual  $T_1$  show good agreement with the parity measurement simulation with a three-component cat state (see Fig. 7). This suggests that the effects of loss in the KPO during the parity measurement can be captured by assuming  $T_{\text{leff}} = 2T_1$ . We believe the factor of 2 in this relationship is coincidental and is specific to the parameters used in this particular simulation. All simulations presented in Fig. 3b include the effect of single-photon loss using  $T_1$  for the state preparation and hold processes, and using  $T_{\text{leff}} (= 2T_1)$  for parity measurement.

### D. Dynamics and relaxation

Now we explore the quantum dynamics of the  $|0_C\rangle$  state, which are associated with the occupation of the excited state  $|0_C^{\text{ex}}\rangle$  and single-photon loss. We first prepared the  $|0_C\rangle$  state following the procedure in Fig. 3a, and then measured Wigner functions at various hold times ( $\tau_{\text{hold}}$ ). From this set of Wigner functions, we extracted the density matrices, which were subsequently used to calculate the mean photon numbers (Fig. 4a) and the fidelities of the qutrit states and the excited states (Fig. 4b).

We observed a strong oscillation in the mean photon number. This oscillation is a consequence of a breathing-like dynamic—an expansion and contraction of the KPO state that eventually approaches the steady state—as clearly shown by the Wigner functions in Fig. 4c. The breathing-like dynamic is primarily caused by oscillation in the relative phase between the  $|0_C\rangle$  and  $|0_C^{\text{ex}}\rangle$  states, rather than in the population. This superposition was inadvertently created by imperfect adiabatic conversion from the  $|0_C\rangle$  and  $|0_C^{\text{ex}}\rangle$  states. Note that the sign of the  $|3n\rangle$  Fock states is opposite between  $|0_C\rangle$  and  $|0_C^{\text{ex}}\rangle$ , with the exception of the  $|0\rangle$  state, as illustrated in Fig. 4d. This accounts for how a small participation from  $|0_C^{\text{ex}}\rangle$  ( $< 4\%$  in population) can lead to mean photon number fluctuations greater than 1, given that the mean photon numbers of the  $|0_C\rangle$  and  $|0_C^{\text{ex}}\rangle$  states are 1.37 and 2.04, respectively (Fig. 4e). Indeed, in Fig. 4b, the population of the  $|0_C^{\text{ex}}\rangle$  state remains  $\lesssim 0.1$  at all times.

One thing worth noting is that the breathing-like

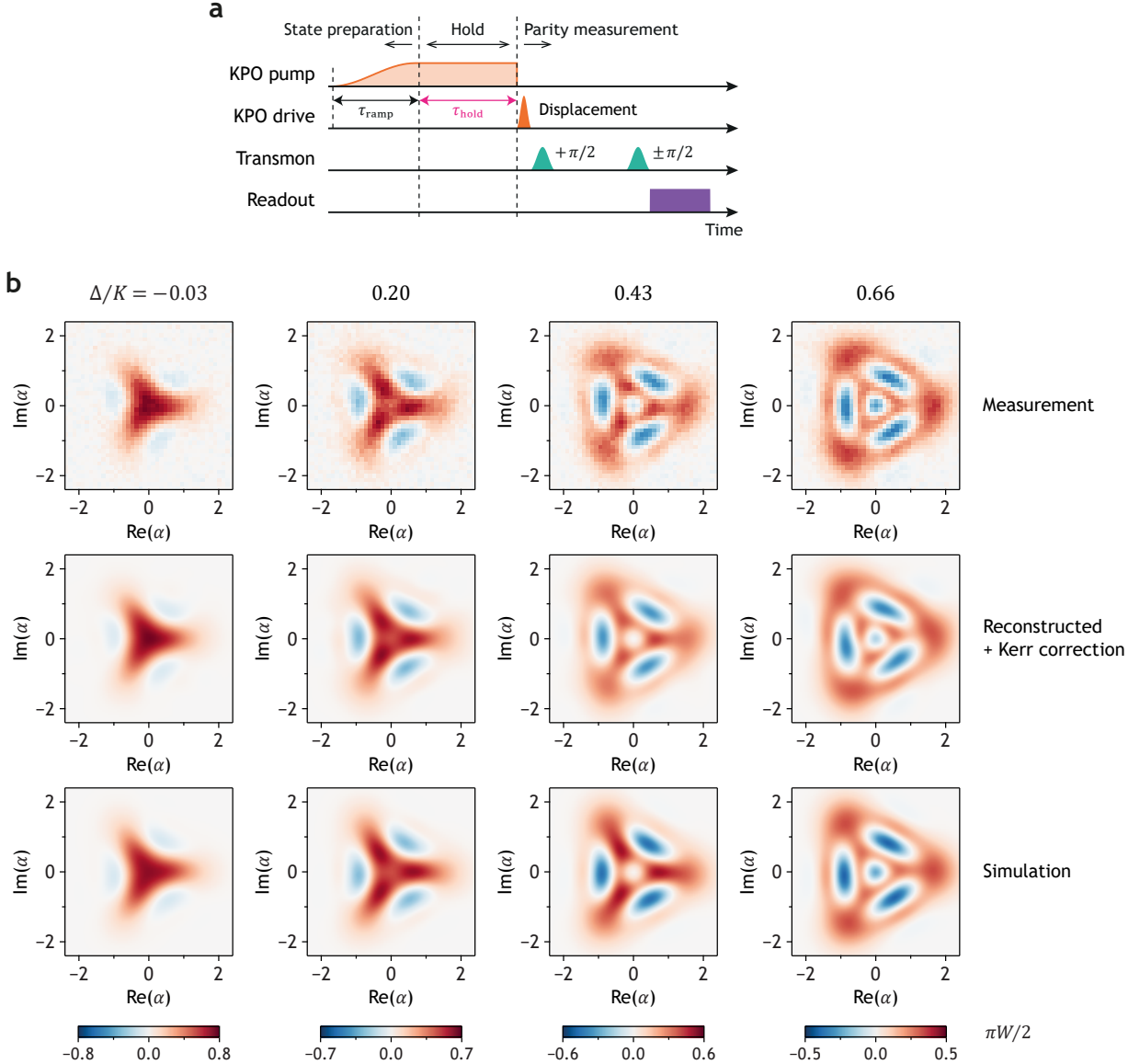


**Fig. 3: Wigner functions of three-photon KPO states.** **a** Pulse sequence for measuring the Wigner function. The pump-pulse conditions are as follows:  $P/K = 0.822$ ,  $P_{\text{CD}}/P = 0.3$ , where  $P_{\text{CD}}$  is the amplitude of the counterdiabatic component of the pump,  $\tau_{\text{ramp}} = 0.4 \mu\text{s}$ , and  $\tau_{\text{hold}} = 0.1 \mu\text{s}$ . **b** Wigner functions of the KPO states for various  $\Delta/K$  values. The measured raw data are shown in the top row, the corresponding reconstructed Wigner functions in the middle row, and the Wigner functions of the simulated states in the bottom row. For the simulations,  $\eta = -0.04$  was used and  $T_1$  was assumed to be  $4 \mu\text{s}$ . From left to right, the mean photon number and fidelity values are: (reconstructed density matrix, simulated density matrix, fidelity) =  $(0.58, 0.52, 0.98)$ ,  $(1.22, 1.06, 0.92)$ ,  $(2.20, 1.99, 0.88)$ , and  $(2.61, 2.60, 0.93)$ .

dynamic, an exotic temporal interference between the qutrit and excited states, is a generic feature of any KPO. An  $n$ -photon KPO ( $n \geq 2$ ) would show similar behaviour under imperfect adiabatic conversion, which results in a superposition between the qudit and excited states. We believe the oscillations in the mean photon number observed in Fig. 4a of Ref. [62] are caused by this interference phenomenon. Consequently, such oscillations serve as a sensitive indicator for population leakage out of the qudit space.

The energy gap between the  $|0_C\rangle$  and  $|0_C^{\text{ex}}\rangle$  states can be directly measured from the frequency of this

oscillation according to the Schrödinger equation:  $|\psi(t)\rangle = \sum_n A_n e^{-iE_n t/\hbar} |\psi_n\rangle$ , where  $A_n$  are complex numbers and the vectors  $|\psi_n\rangle$  are energy eigenstates. We measured this energy gap at three different values of  $\Delta/K$ , which are represented by the stars in Fig. 4f. At  $\Delta/K = 1.114$ , a notable difference is observed between the measured energy gap and the theoretical calculation. This discrepancy may suggest a potential contribution from higher-order terms that are not captured in Eq. (1).

Two consequences of the existence of an energy gap between the qutrit space and the excited states are

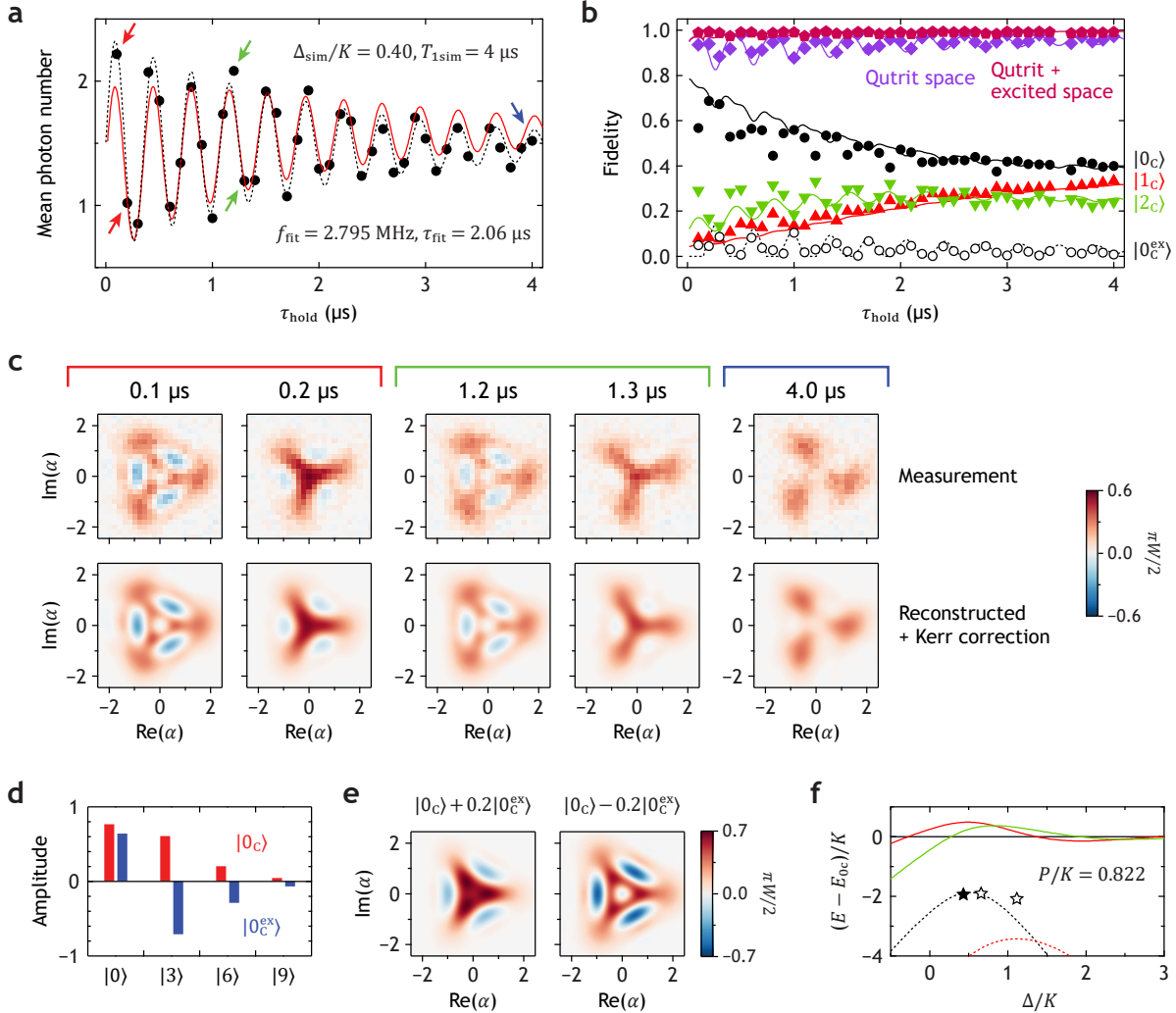


**Fig. 4: Dynamics and relaxation.** **a** Time evolution of the mean photon number, showing oscillations caused by imperfect adiabatic conversion from the  $|0\rangle$  state to the  $|0_C\rangle$  state. The dashed line is a fit to a simple decaying cosine function, with fitted parameters  $f_{\text{fit}}$  and  $\tau_{\text{fit}}$  shown. **b** Time evolution of the fidelity for the qutrit states and  $|0_C^{\text{ex}}\rangle$ . Within the label “Qutrit + excited space,” the excited space refers to the subspace spanned by the states  $|0_C\rangle$ ,  $|1_C\rangle$ , and  $|2_C\rangle$ . In both (a) and (b), the simulation results (solid lines) account for single-photon loss in the KPO during parity measurement using an effective time  $T_{\text{eff}} = 2T_{1\text{sim}}$ . The parameters used for the simulation,  $\Delta_{\text{sim}}$  and  $T_{1\text{sim}}$ , are provided in panel (a). **c** Wigner functions of the KPO state at the times indicated by arrows in (a). **d** The amplitudes of the Fock basis for the  $|0_C\rangle$  and  $|0_C^{\text{ex}}\rangle$  states. **e** Superpositions of the states  $|0_C\rangle$  and  $|0_C^{\text{ex}}\rangle$  with two opposing relative phases. The mean photon number is 0.75 for the state  $|0_C\rangle + 0.2|0_C^{\text{ex}}\rangle$  and 2.03 for  $|0_C\rangle - 0.2|0_C^{\text{ex}}\rangle$ . For (d) and (e),  $\Delta/K = 0.40$ . **f** The first five quasienergy levels  $E$  calculated using Eq. (1). The solid lines indicate the quasienergy levels for the qutrit states: black ( $|0_C\rangle$ ,  $E_{0C}$ ), red ( $|1_C\rangle$ ), and green ( $|2_C\rangle$ ). The dashed lines show the quasienergy levels for the excited states: black ( $|0_C^{\text{ex}}\rangle$ ) and red ( $|1_C^{\text{ex}}\rangle$ ). The stars represent the oscillation frequencies extracted from the mean photon number data; the black solid star specifically corresponds to the frequency determined from the data presented in (a). Here, the energy levels of the excited states are lower than those of the qutrit states, a consequence of the negative sign of  $K$  in Eq. (1). For all simulations in this figure,  $P/K = 0.822$  and  $\eta = -0.04$ .

observed: First, the total population of the qutrit space (represented by the purple diamond symbols in Fig. 4b) shows no decay within our measurement range of  $\tau_{\text{hold}}$ , apart from small oscillations caused by the imperfect adiabatic state preparation. Second, single-photon loss induces a cyclic population transfer within the qutrit space:  $|0_C\rangle \rightarrow |2_C\rangle \rightarrow |1_C\rangle \rightarrow |0_C\rangle \rightarrow \dots$ . Such a cyclic relaxation process is a distinct feature compared to the relaxation in a standard transmon-based qutrit [26]. The data in Fig. 4b

clearly illustrate this process: as  $\tau_{\text{hold}}$  increases, the fidelity of the  $|0_C\rangle$  state decreases. This is followed by an initial increase in the fidelity of the  $|2_C\rangle$  state, which in turn precedes the increase in the population of the  $|1_C\rangle$  state. As the system approaches the steady state, the populations of the qutrit states converge toward similar values.

In Fig. 4b, the fidelity of the  $|0_C\rangle$  and  $|2_C\rangle$  states are oscillating with opposite phases. The oscillation observed in the  $|2_C\rangle$  state can be partly reproduced

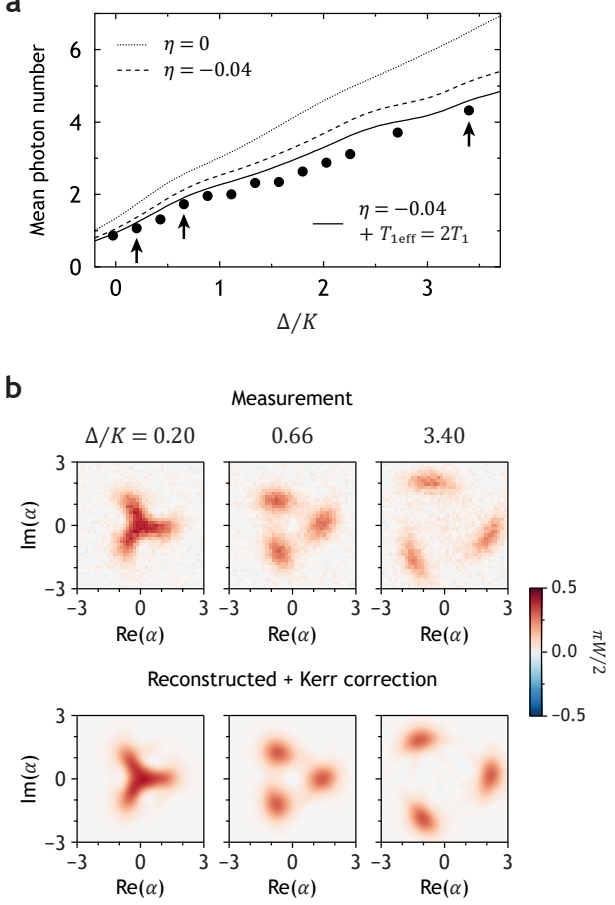


**Fig. 5: Steady states.** **a** The mean photon number of the steady states as a function of the detuning,  $\Delta/K$ . The symbols represent the values extracted from the density matrix reconstructed via Wigner function measurement. The lines are results from the steady-state solution of the Lindblad master equation derived from Eq. (1). The effect of single-photon loss during parity measurement is included in the solid line by using a relaxation time of  $T_1 = 4$   $\mu\text{s}$ . The pump-pulse conditions are as follows:  $P/K = 0.822$ ,  $P_{\text{CD}}/P = 0$ ,  $\tau_{\text{ramp}} = 15$   $\mu\text{s}$ , and  $\tau_{\text{hold}} = 0.2$   $\mu\text{s}$ . A long  $\tau_{\text{ramp}}$  was chosen instead of a long  $\tau_{\text{hold}}$  to eliminate the occupation of excited states and, consequently, to avoid the complex dynamics shown in Fig. 4. **b** Wigner functions of the steady state at the  $\Delta/K$  values indicated by the arrows in (a).

by simulation, suggesting that this dynamic is mainly attributed to the faster relaxation rate of states with a larger mean photon number during the parity measurement (compare Fig. 4a and b). However, the oscillation in the  $|0_C\rangle$  state is not well captured by the simulation. This discrepancy requires further investigation.

### E. Steady states

It is well known that both the noise bias property and the qubit space protection are enhanced as the mean photon number (i.e., the size of the cat state)

increases [14–18]. Thus, to demonstrate our capability for achieving a large mean photon number in this system, we measured the mean photon number of the steady state as a function of the pump detuning  $\Delta/K$  (Fig. 5).

The measured mean photon number increases significantly more slowly than expected from the ideal three-photon KPO model [Eq. (1) with  $\eta = 0$ , dotted line in Fig. 5a]. We find that the higher-order pump term with  $\eta = -0.04$  (dashed line) is primarily responsible for this deviation from the ideal model. Another mechanism we have to consider is single-photon loss during parity measurement. This is relevant because the pump is off during the parity measurement, leaving the qutrit space unprotected. By additionally including this contribution, the final simulation result (solid line) matches the experimental data reasonably well.

## III. DISCUSSION AND CONCLUSION

In this work, we investigated the quantum properties of a three-photon KPO, validating its potential as a protected qutrit platform. We demonstrated quantum coherence by measuring three-photon Rabi oscillations and the characteristic interference patterns with three-fold symmetry (i.e., three-component cat-like states) in Wigner functions. Analysis of the system's time evolution revealed two crucial dynamic features associated with qutrit space protection. First, the oscillation in the mean photon number, caused by temporal interference between the qutrit and excited states, indicates the existence of the energy gap separating the qutrit from the excited states. Second, we observed a unique cyclic population transfer induced by single-photon loss. Furthermore, our investigation of the mean photon number of the steady state as a function of the pump detuning reveals the importance of mitigating the higher-order pump term for maximizing the qutrit space protection.

Future work will focus on exploring the inherent biased-noise properties of this system. A key component for established biased-noise systems is the ability to prepare states autonomously localised in phase space, similar to the coherent states generated in a two-photon KPO. The Wigner functions shown in Fig. 5b suggest that such localised states can be prepared around and above  $\Delta/K = 0.4$  when  $P/K = 0.822$ . Our previous work [12] generated coherent states by preparing the  $|0\rangle + \beta|1\rangle$  state in the Fock basis (where  $\beta$  is a phase factor) and subsequently converting this state to the cat state basis. However, this method is difficult in the three-photon KPO because it requires preparing a state of the form  $|0\rangle + \beta|1\rangle + \gamma|2\rangle$ , making the task of setting the proper phase factors,  $\beta$  and  $\gamma$ , challenging. A more convenient approach for preparing the desired localised state would be measurement-based state preparation, as previously demonstrated in the two-photon KPO [15–18].

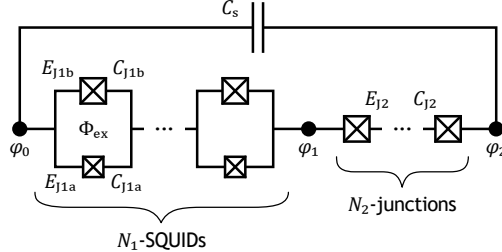


**Fig. 6: Circuit diagram of the KPO.** The KPO consists of  $N_1$  direct-current superconducting quantum interference devices (DC SQUIDs) and a Josephson junction array whose number of junctions is  $N_2$ .  $E_{J1a}$  and  $C_{J1a}$  ( $E_{J1b}$  and  $C_{J1b}$ ) represent the Josephson energy and the capacitance of the smaller (larger) junction in each DC SQUID, respectively.  $C_s$  denotes the shunting capacitance of the KPO, and  $\Phi_{\text{ex}}$  is the external magnetic flux threaded through one DC SQUID.

One potential difficulty for observing the biased-noise properties is that any possible superposition between the qutrit states would be nonstationary. This is because the qutrit states are never energetically degenerate simultaneously unless  $P/K$  or  $\Delta/K$  becomes very large (Fig. 4f). In comparison, the two-photon KPO possesses stationary qubit states when  $\Delta/K$  is a non-negative integer [12]. Since the dynamics of nonstationary qutrit states is unitary, it is reversible in principle. Thus, finding convenient means for generating an effective stationary state will be necessary.

The next crucial experimental milestones involve demonstrating operation of a universal qutrit gate set. Furthermore, extending the platform to implement a protected ququart ( $d = 4$ ) represents another fascinating research direction, particularly given its potential for realising autonomous quantum error correction [63]. Finally, we suggest that a deeper theoretical and experimental investigation into how tunnelling dynamics [64, 65] contribute to relaxation processes in such qudit systems would yield valuable insights for minimizing decoherence across parametrically driven quantum processors.

#### IV. APPENDIX: DERIVATION OF THE HAMILTONIAN

In this section, we derive the Hamiltonian of two interacting Kerr parametric oscillators (KPOs). The circuit diagram is shown in Fig. 6. The Lagrangian of the circuit is given by

$$\mathcal{L} = \mathcal{T} - \mathcal{U},$$

where

$$\begin{aligned} \mathcal{T} &= \left(\frac{\Phi_0}{2\pi}\right)^2 \left[ N_1 \frac{C_{J1a} + C_{J1b}}{2} \left( \frac{\dot{\phi}_1}{N_1} \right)^2 + N_2 \frac{C_{J2}}{2} \left( \frac{\dot{\phi}_2}{N_2} \right)^2 + \frac{C_s}{2} (\dot{\phi}_1 + \dot{\phi}_2)^2 \right], \\ &= \frac{C_1}{2} \dot{\phi}_1^2 + \frac{C_2}{2} \dot{\phi}_2^2 + C_s \dot{\phi}_1 \dot{\phi}_2, \\ \mathcal{U} &= -N_1 E_{J1a} \cos\left(\frac{\phi_1}{N_1} - r_a \varphi_{\text{ex}}\right) - N_1 E_{J1b} \cos\left(\frac{\phi_1}{N_1} + r_b \varphi_{\text{ex}}\right) - N_2 E_{J2} \cos\left(\frac{\phi_2}{N_2}\right). \end{aligned}$$

Here,  $\Phi_0$  is the magnetic flux quantum,  $\phi_1 = \varphi_0 - \varphi_1$ ,  $\phi_2 = \varphi_1 - \varphi_2$ ,  $C_1 \equiv (\Phi_0/2\pi)^2 [C_s + (C_{J1a} + C_{J1b})/N_1]$ ,  $C_2 \equiv (\Phi_0/2\pi)^2 (C_s + C_{J2}/N_2)$ ,  $C_s \equiv (\Phi_0/2\pi)^2 C_s$ ,  $\varphi_{\text{ex}} \equiv 2\pi\Phi_{\text{ex}}/\Phi_0$ , and  $r_a + r_b = 1$ , where these scaling parameters are determined by the irrotational constraint [66]. Note that all capacitances are renormalized by a factor of  $(\Phi_0/2\pi)^2$ .

The conjugate number operators are defined by

$$\hbar N_{\phi 1} = \frac{\partial \mathcal{L}}{\partial \dot{\phi}_1} = C_1 \dot{\phi}_1 + C_s \dot{\phi}_2, \quad \hbar N_{\phi 2} = \frac{\partial \mathcal{L}}{\partial \dot{\phi}_2} = C_s \dot{\phi}_1 + C_2 \dot{\phi}_2,$$

where the reduced Planck constants are inserted to make  $N_{\phi 1}$  and  $N_{\phi 2}$  dimensionless. In matrix form,

$$\hbar \begin{pmatrix} N_{\phi 1} \\ N_{\phi 2} \end{pmatrix} = \begin{pmatrix} C_1 & C_s \\ C_s & C_2 \end{pmatrix} \begin{pmatrix} \dot{\phi}_1 \\ \dot{\phi}_2 \end{pmatrix}.$$

Using the inverse capacitance matrix, we obtain

$$\begin{pmatrix} \dot{\phi}_1 \\ \dot{\phi}_2 \end{pmatrix} = \frac{\hbar}{C_1 C_2 - C_s^2} \begin{pmatrix} C_2 & -C_s \\ -C_s & C_1 \end{pmatrix} \begin{pmatrix} N_{\phi 1} \\ N_{\phi 2} \end{pmatrix}.$$

With the matrix above, and using the formula  $A \cos(x) + B \sin(x) = R \cos(x - \lambda)$ , where  $R = \sqrt{A^2 + B^2}$  and  $\tan(\lambda) = B/A$ , we obtain

$$\mathcal{H} = 4E_{C1}N_{\phi 1}^2 + 4E_{C2}N_{\phi 2}^2 - 8E_{Cs}N_{\phi 1}N_{\phi 2} - N_1E_{J1}^{\text{mod}}(\varphi_{\text{ex}}) \cos\left(\frac{\phi_1}{N_1} - \lambda(\varphi_{\text{ex}})\right) - N_2E_{J2} \cos\left(\frac{\phi_2}{N_2}\right), \quad (3)$$

where

$$\begin{aligned} E_{C1} &\equiv \frac{\hbar^2 C_2}{8(C_1 C_2 - C_s^2)}, \quad E_{C2} \equiv \frac{\hbar^2 C_1}{8(C_1 C_2 - C_s^2)}, \quad E_{Cs} \equiv \frac{\hbar^2 C_s}{8(C_1 C_2 - C_s^2)}, \\ E_{J1}^{\text{mod}}(\varphi_{\text{ex}}) &= \sqrt{E_{J1a}^2 + E_{J1b}^2 + 2E_{J1a}E_{J1b} \cos(\varphi_{\text{ex}})}, \\ \lambda(\varphi_{\text{ex}}) &= \arctan\left(\frac{E_{J1a} \sin(r_a \varphi_{\text{ex}}) - E_{J1b} \sin(r_b \varphi_{\text{ex}})}{E_{J1a} \cos(r_a \varphi_{\text{ex}}) + E_{J1b} \cos(r_b \varphi_{\text{ex}})}\right). \end{aligned}$$

So far, no approximation has been introduced.

To account for the flux-bias modulation, we decompose  $\varphi_{\text{ex}}$  and  $\lambda$  into static and oscillating parts, i.e.,  $\varphi_{\text{dc}} + \varphi_{\text{ac}}(t)$  and  $\lambda_{\text{dc}} + \lambda_{\text{ac}}(t)$ . The oscillating part is the parametric pump given by  $\varphi_{\text{ac}}(t) = 2\varphi_{\text{ac}}^{(0)} \cos(\omega_p t)$  and  $\lambda_{\text{ac}}(t) = 2\lambda_{\text{ac}}^{(0)} \cos(\omega_p t)$ , where  $\omega_p$  is the frequency of the pump applied to the KPO. Then, we introduce a variable change,  $\phi_{\text{dc}} \rightarrow \phi_{\text{dc}} + N_1 \lambda_{\text{dc}}$ . Since  $\varphi_{\text{ac}}^{(0)} \ll 2\pi$ , we take the Taylor expansion at  $\varphi_{\text{ex}} = \varphi_{\text{dc}}$ :

$$\mathcal{U} \approx -N_1 \left( E_{J1}^{(0)} + E_{J1}^{(1)} \varphi_{\text{ac}} + E_{J1}^{(2)} \varphi_{\text{ac}}^2 \right) \cos\left(\frac{\phi_1}{N_1} + \lambda_{\text{ac}}\right) - N_2 E_{J2} \cos\left(\frac{\phi_2}{N_2}\right), \quad (4)$$

where

$$\begin{aligned} E_{J1}^{(0)} &= \sqrt{E_{J1a}^2 + E_{J1b}^2 + 2E_{J1a}E_{J1b} \cos(\varphi_{\text{dc}})}, \\ E_{J1}^{(1)} &= -\frac{1}{E_{J1}^{(0)}} E_{J1a}E_{J1b} \sin(\varphi_{\text{dc}}), \\ E_{J1}^{(2)} &= -\frac{1}{2(E_{J1}^{(0)})^3} \left\{ E_{J1a}E_{J1b}(E_{J1a}^2 + E_{J1b}^2) \cos(\varphi_{\text{dc}}) + (E_{J1a}E_{J1b})^2 [\cos^2(\varphi_{\text{dc}}) + 1] \right\}. \end{aligned}$$

Here, the  $\varphi_{\text{ac}}^2$  terms induce a small frequency shift, which we refer to as an AC Stark-like frequency shift for convenience. The  $E_{J1}^{(1)} \varphi_{\text{ac}}$  term will be ignored because the terms associated with it disappear after the rotating-wave approximation; the majority of three-photon pump comes from  $\lambda_{\text{ac}}$  as shown below [42].

Since  $\lambda_{\text{ac}} \ll 2\pi$ , we can expand Eq. (4) further:

$$\begin{aligned} \mathcal{U} &= -N_1 \left( E_{J1}^{(0)} + E_{J1}^{(2)} \varphi_{\text{ac}}^2 \right) \left[ \cos\left(\frac{\phi_1}{N_1}\right) \cos(\lambda_{\text{ac}}) - \sin\left(\frac{\phi_1}{N_1}\right) \sin(\lambda_{\text{ac}}) \right] - N_2 E_{J2} \cos\left(\frac{\phi_2}{N_2}\right) \\ &\approx -N_1 \left( E_{J1}^{(0)} + E_{J1}^{(2)} \varphi_{\text{ac}}^2 \right) \left[ \cos\left(\frac{\phi_1}{N_1}\right) - \lambda_{\text{ac}} \sin\left(\frac{\phi_1}{N_1}\right) \right] - N_2 E_{J2} \cos\left(\frac{\phi_2}{N_2}\right) \\ &\approx -N_1 \left( E_{J1}^{(0)} + E_{J1}^{(2)} \varphi_{\text{ac}}^2 \right) \left\{ 1 - \frac{1}{2} \left( \frac{\phi_1}{N_1} \right)^2 + \frac{1}{24} \left( \frac{\phi_1}{N_1} \right)^4 - \lambda_{\text{ac}} \left[ \left( \frac{\phi_1}{N_1} \right) - \frac{1}{6} \left( \frac{\phi_1}{N_1} \right)^3 + \frac{1}{120} \left( \frac{\phi_1}{N_1} \right)^5 \right] \right\} \\ &\quad - N_2 E_{J2} \left[ 1 - \frac{1}{2} \left( \frac{\phi_2}{N_2} \right)^2 + \frac{1}{24} \left( \frac{\phi_2}{N_2} \right)^4 \right] \\ &\approx -N_1 E_{J1} \left[ 1 - \frac{1}{2} \left( \frac{\phi_1}{N_1} \right)^2 + \frac{1}{24} \left( \frac{\phi_1}{N_1} \right)^4 \right] - N_2 E_{J2} \left[ 1 - \frac{1}{2} \left( \frac{\phi_2}{N_2} \right)^2 + \frac{1}{24} \left( \frac{\phi_2}{N_2} \right)^4 \right] \\ &\quad + 2\gamma \cos(\omega_p t) \left[ \left( \frac{\phi_1}{N_1} \right) - \frac{1}{6} \left( \frac{\phi_1}{N_1} \right)^3 + \frac{1}{120} \left( \frac{\phi_1}{N_1} \right)^5 \right], \end{aligned}$$

where  $E_{J1} \equiv E_{J1}^{(0)} + 2E_{J1}^{(2)} (\varphi_{\text{ac}}^{(0)})^2$  and  $\gamma \equiv N_1 E_{J1}^{(0)} \lambda_{\text{ac}}^{(0)}$ . The  $\varphi_{\text{ac}}^2$  term is averaged out by using  $\langle \varphi_{\text{ac}}^2 \rangle = 2(\varphi_{\text{ac}}^{(0)})^2$  and absorbed into  $E_{J1}$ .

We introduce an approximation to reduce the number of phase variables into one:  $\phi_2/\phi_1 = N_2 E_{J2}/(N_1 E_{J1}) \equiv \xi$ , i.e.,  $\phi_2 = \xi \phi_1$ . Then, we introduce a new variable,  $\phi \equiv \phi_1 + \phi_2$ , which gives  $\phi_1 = \phi/(1+\xi)$  and  $\phi_2 = \phi \xi/(1+\xi)$ .

$\xi$ ), and the conjugate number  $N_\phi$ . After replacing variables, we obtain a single-phase-variable Hamiltonian (hereafter, we add a hat to an operator for clarity),

$$\hat{\mathcal{H}} = 4E_C \hat{N}_\phi^2 + \frac{1}{2} E_K \hat{\phi}^2 - N_1 E_{J1} \left[ 1 + \frac{1}{24} \left( \frac{\hat{\phi}}{(1+\xi)N_1} \right)^4 \right] - N_2 E_{J2} \left[ 1 + \frac{1}{24} \left( \frac{\xi \hat{\phi}}{(1+\xi)N_2} \right)^4 \right] \\ + 2\gamma \cos(\omega_p t) \left[ \left( \frac{\hat{\phi}}{(1+\xi)N_1} \right) - \frac{1}{6} \left( \frac{\hat{\phi}}{(1+\xi)N_1} \right)^3 + \frac{1}{120} \left( \frac{\hat{\phi}}{(1+\xi)N_1} \right)^5 \right],$$

where

$$E_C \equiv \frac{\hbar^2}{8 \left[ C_1 \left( \frac{1}{1+\xi} \right)^2 + C_2 \left( \frac{\xi}{1+\xi} \right)^2 + C_s \frac{2\xi}{(1+\xi)^2} \right]}, \quad E_K = \frac{1}{(1+\xi)^2} \left( \frac{E_{J1}}{N_1} + \frac{\xi^2 E_{J2}}{N_2} \right).$$

Since  $C_s \gg C_{J1a}, C_{J1b}, C_{J2}$  in our circuit,  $E_C \approx e^2/(2C_s)$ , where  $e$  is the electron charge.

We move to the occupation-number representation by defining

$$\hat{N}_\phi = i N_\phi^{(0)} (\hat{a}^\dagger - \hat{a}) \quad \text{and} \quad \hat{\phi} = \phi^{(0)} (\hat{a}^\dagger + \hat{a}),$$

where  $N_\phi^{(0)} = \sqrt[4]{E_K/32E_C}$  and  $\phi^{(0)} = \sqrt[4]{2E_C/E_K}$  are the zero-point fluctuations. Then we have

$$\hat{\mathcal{H}} = \hbar \omega_K^{(0)} \hat{a}^\dagger \hat{a} - N_1 E_{J1} \left[ 1 + \frac{1}{24} \left( \frac{\hat{\phi}}{(1+\xi)N_1} \right)^4 \right] - N_2 E_{J2} \left[ 1 + \frac{1}{24} \left( \frac{\xi \hat{\phi}}{(1+\xi)N_2} \right)^4 \right] \\ + 2\gamma \cos(\omega_p t) \left[ \left( \frac{\hat{\phi}}{(1+\xi)N_1} \right) - \frac{1}{6} \left( \frac{\hat{\phi}}{(1+\xi)N_1} \right)^3 + \frac{1}{120} \left( \frac{\hat{\phi}}{(1+\xi)N_1} \right)^5 \right],$$

where  $\hbar \omega_K^{(0)} \equiv \sqrt{8E_C E_K}$ .

We move to the rotating frame whose Hamiltonian is defined by  $\hat{\mathcal{H}}_0/\hbar = (\omega_p/3)\hat{a}^\dagger \hat{a}$  and make the rotating-wave approximation. By using the formula (derived on the basis of Ref. [67])

$$(\hat{a}^\dagger \pm \hat{a})^n = \sum_{k=0}^n \sum_{m=0}^{\lfloor \frac{k}{2} \rfloor} \frac{(\pm 1)^{m-k} n!}{(n-k)! (k-2m)! m! 2^m} (\hat{a}^\dagger)^{k-2m} \hat{a}^{n-k},$$

we obtain

$$-\frac{1}{(1+\xi)^4} \left( \frac{E_{J1}}{N_1^3} + \frac{\xi^4 E_{J2}}{N_2^3} \right) \frac{\hat{\phi}^4}{24} \Rightarrow -\hbar K \hat{a}^\dagger \hat{a} - \frac{\hbar K}{2} \hat{a}^\dagger \hat{a}^\dagger \hat{a} \hat{a} \\ - \frac{\gamma}{3(1+\xi)^3 N_1^3} \cos(\omega_p t) \hat{\phi}^3 \Rightarrow \hbar \frac{P}{2} (\hat{a}^\dagger \hat{a}^\dagger \hat{a}^\dagger + \hat{a} \hat{a} \hat{a}), \\ \frac{\gamma}{60(1+\xi)^5 N_1^5} \cos(\omega_p t) \hat{\phi}^5 \Rightarrow \hbar \frac{P}{2} \eta (\hat{a}^\dagger \hat{a}^\dagger \hat{a}^\dagger \hat{a}^\dagger \hat{a} + \hat{a}^\dagger \hat{a} \hat{a} \hat{a} \hat{a}),$$

where

$$\hbar K \equiv \frac{1}{(1+\xi)^4} \left( \frac{E_{J1}}{N_1^3} + \frac{\xi^4 E_{J2}}{N_2^3} \right) \frac{E_C}{E_K}, \quad \hbar P \equiv -\frac{E_{J1}^{(0)} \lambda_{ac}^{(0)}}{3(1+\xi)^3 N_1^2} \left( \frac{2E_C}{E_K} \right)^{3/4}, \quad \eta \equiv -\frac{1}{4(1+\xi)^2 N_1^2} \sqrt{\frac{2E_C}{E_K}}. \quad (5)$$

The final Hamiltonian is

$$\hat{\mathcal{H}}_{\text{rot}}/\hbar \approx \Delta \hat{a}^\dagger \hat{a} - \frac{K}{2} \hat{a}^\dagger \hat{a}^\dagger \hat{a} \hat{a} + \frac{P}{2} [(\hat{a}^\dagger \hat{a}^\dagger \hat{a}^\dagger + \hat{a} \hat{a} \hat{a}) + \eta (\hat{a}^\dagger \hat{a}^\dagger \hat{a}^\dagger \hat{a}^\dagger \hat{a} + \hat{a}^\dagger \hat{a} \hat{a} \hat{a} \hat{a})], \quad (6)$$

where  $\Delta (\equiv \omega_K - \omega_p/3)$  is the KPO-pump frequency detuning, where  $\omega_K (\equiv \omega_K^{(0)} - K)$  is the transition frequency between the  $|0\rangle$  and  $|1\rangle$  states. Note that Eq. (6) is the same as Eq. (1).

**Table I: Measured system parameters.**  $\Phi_0$  is the magnetic flux quantum. For the self-Kerr coefficient of the KPOs, the value in parentheses is the coefficient when the pump is on. The Hamiltonian was characterized by analysing Rabi oscillations in the  $|0\rangle$  state population, following the methodology outlined in Ref. [12].

Physical quantity	Symbol	Value
Number of DC SQUIDs in KPO	$N_1$	2
Number of junctions in junction array	$N_2$	4
Junction asymmetry factor of DC SQUID (design value)	$E_{J1b}/E_{J1a}$	1.4
Josephson energy of junctions in junction array (design value)	$E_{J1b}/E_{J2}$	1.0
External magnetic flux threaded through one DC SQUID	$\Phi_{\text{ex}}$	$0.149\Phi_0$
Transition frequency between the $ 0\rangle$ and $ 1\rangle$ states of KPO	$\omega_K/2\pi$	3.112 GHz
Self-Kerr coefficient of KPO	$K/2\pi$	1.70 (1.46) MHz
Longitudinal relaxation time of KPO	$T_1^K$	4.5 $\mu$ s
Transverse relaxation time of KPO	$T_2^K$	5.3 $\mu$ s
Transition frequency between $ g\rangle$ and $ e\rangle$ states of transmon	$\omega_T/2\pi$	5.3237 GHz
Anharmonicity of transmon	$K_T/2\pi$	173.0 MHz
Longitudinal relaxation time of transmon	$T_1^T$	9.2 $\mu$ s
Transverse relaxation time of transmon	$T_2^T$	5.0 $\mu$ s
Cross-Kerr coefficient between KPO and transmon	$\chi_{KT}/2\pi$	0.79 MHz
Number of thermally excited photons in KPO	$n_{\text{th}}$	0.04
Resonance frequency of readout resonator	$\omega_R/2\pi$	7.4866 GHz
Cross-Kerr coefficient between transmon and readout resonator	$\chi_{TR}/2\pi$	2.53 MHz

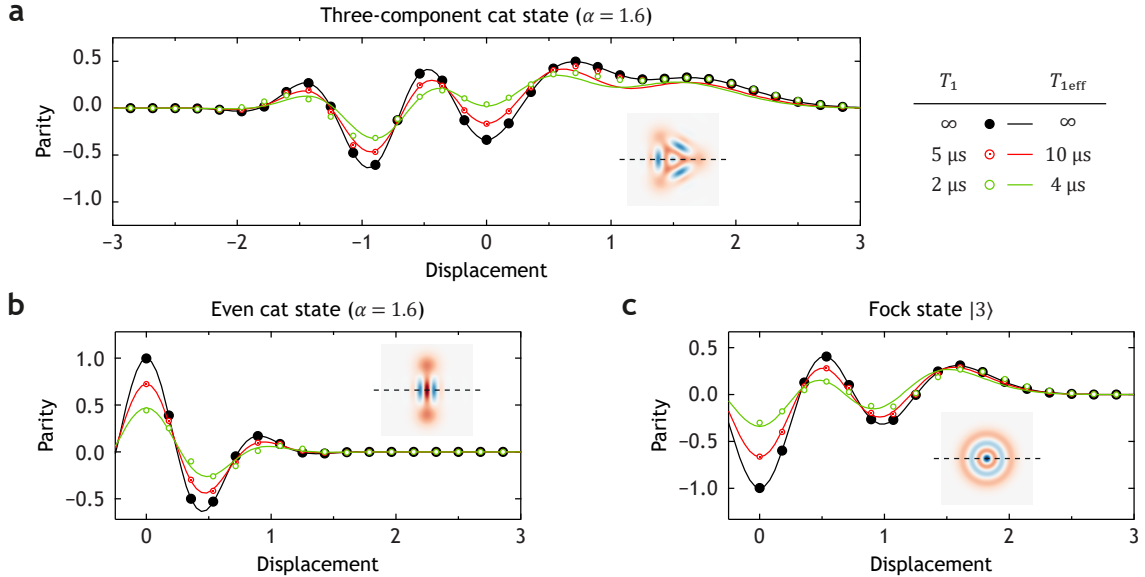


**Fig. 7: Effect of single-photon loss in the KPO during parity measurement.** The states under investigation are as follows: **a** three-component cat state with  $\alpha = 1.6$ ; **b** even cat state with  $\alpha = 1.6$ ; **c** Fock state  $|3\rangle$ . The insets show Wigner functions within the displacement  $\pm 3$  range in the absence of loss. The symbols correspond to a simulated parity measurement taken along the dashed line, while the solid lines represent the linecut of the Wigner function (taken along the dashed line in the inset) for a decayed state with an effective  $T_1$ , denoted  $T_{1\text{eff}}$ .

## ACKNOWLEDGMENTS

The authors thank Akiyoshi Tomonaga of the National Institute of Advanced Industrial Science and Technology for providing niobium films, the Semiconductor Science Research Support Team in RIKEN for technical support on fabrication, and the MIT Lincoln Laboratory for providing a Josephson travelling-wave

parametric amplifier. This work was supported by the Japan Science and Technology Agency (Moonshot R&D, JPMJMS2067) and the New Energy and Industrial Technology Development Organization (NEDO, JPNP16007).

SK and JST conceived the project. SK, DH, TN, HM, and JST designed the details of the experiment. SK performed the measurements and data analysis

with contributions from DH, TN, KT, and RK. SW provided theoretical support. DH and KT wrote the software for the measurements. HM managed the hardware. YZ and HM designed and prepared the sample package. SK designed the chip. TN, DS, and RK fabricated the chip. SK wrote the original draft. All authors contributed to the review and editing of the paper. SK, FY, and JST supervised the project. JST secured the funding.

The authors declare that they have no competing interests.

## REFERENCES

- [1] A. Blais, A. L. Grimsmo, S. M. Girvin, and A. Wallraff, *Circuit quantum electrodynamics*, Rev. Mod. Phys. **93**, 025005 (2021).
- [2] S. Kwon, A. Tomonaga, G. Lakshmi Bhai, S. J. Devitt, and J.-S. Tsai, *Gate-based superconducting quantum computing*, J. Appl. Phys. **129**, 041102 (2021).
- [3] P. Krantz, M. Kjaergaard, F. Yan, T. P. Orlando, S. Gustavsson, and W. D. Oliver, *A quantum engineer's guide to superconducting qubits*, Appl. Phys. Rev. **6**, 021318 (2019).
- [4] X. Gu, A. F. Kockum, A. Miranowicz, Y.-x. Liu, and F. Nori, *Microwave photonics with superconducting quantum circuits*, Phys. Rep. **718–719**, 1 (2017).
- [5] B. M. Terhal, J. Conrad, and C. Vuillot, *Towards scalable bosonic quantum error correction*, Quantum Sci. Technol. **5**, 043001 (2020).
- [6] W. Cai, Y. Ma, W. Wang, C.-L. Zou, and L. Sun, *Bosonic quantum error correction codes in superconducting quantum circuits*, Fundam. Res. **1**, 50 (2021).
- [7] A. Joshi, K. Noh, and Y. Y. Gao, *Quantum information processing with bosonic qubits in circuit QED*, Quantum Sci. Technol. **6**, 033001 (2021).
- [8] W.-L. Ma, S. Puri, R. J. Schoelkopf, M. H. Devoret, S. M. Girvin, and L. Jiang, *Quantum control of bosonic modes with superconducting circuits*, Sci. Bull. **66**, 1789 (2021).
- [9] M. Dykman, in *Fluctuating Nonlinear Oscillators: From Nanomechanics to Quantum Superconducting Circuits*, edited by M. Dykman (Oxford University Press, 2012).
- [10] H. Goto, *Quantum computation based on quantum adiabatic bifurcations of Kerr-nonlinear parametric oscillators*, J. Phys. Soc. Jpn. **88**, 061015 (2019).
- [11] W. Wustmann and V. Shumeiko, *Parametric effects in circuit quantum electrodynamics*, Low Temp. Phys. **45**, 848–869 (2019).
- [12] D. Iyama, T. Kamiya, S. Fujii, H. Mukai, Y. Zhou, T. Nagase, A. Tomonaga, R. Wang, J.-J. Xue, S. Watabe, S. Kwon, and J.-S. Tsai, *Observation and manipulation of quantum interference in a superconducting Kerr parametric oscillator*, Nat. Commun. **15**, 86 (2024).
- [13] D. Hoshi, T. Nagase, S. Kwon, D. Iyama, T. Kamiya, S. Fujii, H. Mukai, S. Ahmed, A. F. Kockum, S. Watabe, F. Yoshihara and J.-S. Tsai, *Entangling Schrödinger's cat states by bridging discrete-and continuous-variable encoding*, Nat. Commun. **16**, 1309 (2025).
- [14] A. Grimm, N. E. Frattini, S. Puri, S. O. Mundhada, S. Touzard, M. Mirrahimi, S. M. Girvin, S. Shankar, and M. H. Devoret, *Stabilization and operation of a Kerr-cat qubit*, Nature **584**, 205 (2020).
- [15] A. Hajr, B. Qing, K. Wang, G. Koolstra, Z. Pedramrazi, Z. Kang, L. Chen, L. B. Nguyen, C. Jünger, N. Goss, I. Huang, B. Bhandari, N. E. Frattini, S. Puri, J. Dressel, A. N. Jordan, D. I. Santiago, and I. Siddiqi, *High-Coherence Kerr-Cat Qubit in 2D Architecture*, Phys. Rev. X **14**, 041049 (2024).
- [16] B. Qing, A. Hajr, K. Wang, G. Koolstra, L. B. Nguyen, J. Hines, I. Huang, B. Bhandari, L. Chen, Z. Kang, C. Jünger, N. Goss, N. Jain, H. Kim, K.-H. Lee, A. Hashim, N. E. Frattini, Z. Pedramrazi, J. Dressel, A. N. Jordan, D. I. Santiago, and I. Siddiqi, *Quantum Benchmarking of High-Fidelity Noise-Biased Operations on a Detuned-Kerr-Cat Qubit*, arXiv:2411.04442
- [17] N. E. Frattini, R. G. Cortiñas, J. Venkatraman, X. Xiao, Q. Su, C. U Lei, B. J. Chapman, V. R. Joshi, S. M. Girvin, R. J. Schoelkopf, S. Puri, and M. H. Devoret, *Observation of Pairwise Level Degeneracies and the Quantum Regime of the Arrhenius Law in a Double-Well Parametric Oscillator*, Phys. Rev. X **14**, 031040 (2024).
- [18] J. Venkatraman, R. G. Cortiñas, N. E. Frattini, and M. H. Devoret, *A driven Kerr oscillator with two-fold degeneracies for qubit protection*, Proc. Natl. Acad. Sci. U. S. A. **121**, e2311241121 (2024).
- [19] A. Z. Ding, B. L. Brock, A. Eickbusch, A. Koottandavida, N. E. Frattini, R. G. Cortiñas, V. R. Joshi, S. J. de Graaf, B. J. Chapman, S. Ganjam, L. Frunzio, R. J. Schoelkopf, and M. H. Devoret, *Quantum control of an oscillator with a Kerr-cat qubit*, Nat. Commun. **16**, 5279 (2025).
- [20] A. S. Darmawan, B. J. Brown, A. L. Grimsmo, D. K. Tuckett, and S. Puri, *Practical Quantum Error Correction with the XZZX Code and Kerr-Cat Qubits*, PRX Quantum **2**, 030345 (2021).
- [21] B. P. Lanyon, M. Barbieri, M. P. Almeida, T. Jennewein, T. C. Ralph, K. J. Resch, G. J. Pryde, J. L. O'Brien, A. Gilchrist, and A. G. White, *Simplifying quantum logic using higher-dimensional Hilbert spaces*, Nature Phys. **5**, 134 (2009).
- [22] E. T. Campbell, *Enhanced Fault-Tolerant Quantum Computing in d-Level Systems*, Phys. Rev. Lett. **113**, 230501 (2014).
- [23] Y. Wang, Z. Hu, B. C. Sanders, and S. Kais, *Qudits and High-Dimensional Quantum Computing*, Front. Phys. **8**, 589504 (2020).
- [24] E. O. Kiktenko, A. S. Nikolaeva, and A. K. Fedorov, *Colloquium: Qudits for decomposing multiqubit gates and realizing quantum algorithms*, Rev. Mod. Phys. **97**, 021003 (2025).
- [25] M. S. Blok, V. V. Ramasesh, T. Schuster, K. O'Brien, J. M. Kreikebaum, D. Dahmen, A. Morvan, B. Yoshida, N. Y. Yao, and I. Siddiqi, *Quantum Information Scrambling on a Superconducting Qutrit Processor*,

- Phys. Rev. X **11**, 021010 (2021).
- [26] A. Morvan, V. V. Ramasesh, M. S. Blok, J. M. Kreikebaum, K. O'Brien, L. Chen, B. K. Mitchell, R. K. Naik, D. I. Santiago, and I. Siddiqi, *Qutrit Randomized Benchmarking*, Phys. Rev. Lett. **126**, 210504 (2021).
- [27] M. Kononenko, M. A. Yurtalan, S. Ren, J. Shi, S. Ashhab, and A. Lupascu, *Characterization of control in a superconducting qutrit using randomized benchmarking*, Phys. Rev. Research **3**, L042007 (2021).
- [28] N. Goss, A. Morvan, B. Marinelli, B. K. Mitchell, L. B. Nguyen, R. K. Naik, L. Chen, C. Jünger, J. M. Kreikebaum, D. I. Santiago, J. J. Wallman, and I. Siddiqi, *High-fidelity qutrit entangling gates for superconducting circuits*, Nat. Commun. **13**, 7481 (2022).
- [29] K. Luo, W. Huang, Z. Tao, L. Zhang, Y. Zhou, J. Chu, W. Liu, B. Wang, J. Cui, S. Liu, F. Yan, M.-H. Yung, Y. Chen, T. Yan, and D. Yu, *Experimental Realization of Two Qutrits Gate with Tunable Coupling in Superconducting Circuits*, Phys. Rev. Lett. **130**, 030603 (2023).
- [30] T. Roy, Z. Li, E. Kapit, and D. I. Schuster, *Two-Qutrit Quantum Algorithms on a Programmable Superconducting Processor*, Phys. Rev. Applied **19**, 064024 (2023).
- [31] N. Goss, S. Ferracin, A. Hashim, A. Carignan-Dugas, J. M. Kreikebaum, R. K. Naik, D. I. Santiago, and I. Siddiqi, *Extending the computational reach of a superconducting qutrit processor*, npj Quantum Inf. **10**, 101 (2024).
- [32] K. Zhou, J.-W. Xu, Q.-P. Su, Y. Zhang, X.-M. Yu, Z. Ma, H.-Y. Zhang<sup>1</sup>, H.-Y. Shi, W. Zheng, S. Pan, Y. Kang, Z. Huang, C.-P. Yang, S.-X. Li, and Y. Yu, *Demonstration of Discrete-Time Quantum Walks and Observation of Topological Edge States in a Superconducting Qutrit Chain*, Phys. Rev. Lett. **135**, 250601 (2025).
- [33] Z. Wang, R. W. Parker, E. Champion, and M. S. Blok, *High- $E_J/E_C$  transmon qudits with up to 12 levels*, Phys. Rev. Applied **23**, 034046 (2025).
- [34] E. Champion, Z. Wang, R. W. Parker, and M. S. Blok, *Efficient Control of a Transmon Qudit Using Effective Spin-7/2 Rotations*, Phys. Rev. X **15**, 021096 (2025).
- [35] B. L. Brock, S. Singh, A. Eickbusch, V. V. Sivak, A. Z. Ding, L. Frunzio, S. M. Girvin, and M. H. Devoret, *Quantum error correction of qudits beyond break-even*, Nature **641**, 612 (2025).
- [36] B. Vlastakis, G. Kirchmair, Z. Leghtas, S. E. Nigg, L. Frunzio, S. M. Girvin, M. Mirrahimi, M. H. Devoret, and R. J. Schoelkopf, *Deterministically Encoding Quantum Information Using 100-Photon Schrödinger Cat States*, Science **342**, 607–610 (2013).
- [37] X. L. He, Y. Lu, D. Q. Bao, H. Xue, W. B. Jiang, Z. Wang, A. F. Roudsari, P. Delsing, J. S. Tsai, and Z. R. Lin, *Fast generation of Schrödinger cat states using a Kerr-tunable superconducting resonator*, Nat. Commun. **14**, 6358 (2023).
- [38] S. L. Braunstein and R. I. McLachlan, *Generalized squeezing*, Phys. Rev. A **35**, 1659 (1987).
- [39] K. Banaszek and P. L. Knight, *Quantum interference in three-photon down-conversion*, Phys. Rev. A **55**, 2368 (1997).
- [40] T. Felbinger, S. Schiller, and J. Mlynek, *Oscillation and Generation of Nonclassical States in Three-Photon Down-Conversion*, Phys. Rev. Lett. **80**, 492 (1998).
- [41] F. Dell'Anno, S. De Siena, and F. Illuminati, *Multiphoton quantum optics and quantum state engineering*, Phys. Rep. **428**, 53 (2006).
- [42] C. W. S. Chang, C. Sabín, P. Forn-Díaz, F. Quijandría, A. M. Vadiraj, I. Nsanzineza, G. Johansson, and C. M. Wilson, *Observation of Three-Photon Spontaneous Parametric Down-Conversion in a Superconducting Parametric Cavity*, Phys. Rev. X **10**, 011011 (2020).
- [43] A. M. Eriksson, T. Sépulcre, M. Kervinen, T. Hillmann, M. Kudra, S. Dupouy, Y. Lu, M. Khanahmadi, J. Yang, C. Castillo-Moreno, P. Delsing, and S. Gasparinetti, *Universal control of a bosonic mode via drive-activated native cubic interactions*, Nat. Commun. **15**, 2512 (2024).
- [44] I.-M. Svensson, A. Bengtsson, P. Krantz, J. Bylander, V. Shumeiko, and P. Delsing, *Period-tripling subharmonic oscillations in a driven superconducting resonator*, Phys. Rev. B **96**, 174503 (2017).
- [45] I.-M. Svensson, A. Bengtsson, J. Bylander, V. Shumeiko, and P. Delsing, *Period multiplication in a parametrically driven superconducting resonator*, Appl. Phys. Lett. **113**, 022602 (2018).
- [46] Y. Zhang, J. Gosner, S. M. Girvin, J. Ankerhold, and M. I. Dykman, *Time-translation-symmetry breaking in a driven oscillator: From the quantum coherent to the incoherent regime*, Phys. Rev. A **96**, 052124 (2017).
- [47] Y. Zhang and M. I. Dykman, *Nonlocal random walk over Floquet states of a dissipative nonlinear oscillator*, Phys. Rev. E **100**, 052148 (2019).
- [48] Y. Tadokoro, H. Tanaka, and M. I. Dykman, *Noise-induced switching from a symmetry-protected shallow metastable state*, Sci. Rep. **10**, 10413 (2020).
- [49] J. Gosner, B. Kubala, and J. Ankerhold, *Relaxation dynamics and dissipative phase transition in quantum oscillators with period tripling*, Phys. Rev. B **101**, 054501 (2020).
- [50] B. Lang and A. D. Armour, *Multi-photon resonances in Josephson junction-cavity circuits*, New J. Phys. **23**, 033021 (2021).
- [51] L. Arndt and F. Hassler, *Period Tripling due to Parametric Down-Conversion in Circuit QED*, Phys. Rev. Lett. **128**, 187701 (2022).
- [52] F. Minganti, V. Savona, and A. Biella, *Dissipative phase transitions in n-photon driven quantum nonlinear resonators*, Quantum **7**, 1170 (2023).
- [53] F. Iachello, R. G. Cortiñas, F. Pérez-Bernal, and L. F. Santos, *Symmetries of the squeeze-driven Kerr oscillator*, J. Phys. A: Math. Theor. **56**, 495305 (2023).
- [54] L. Guo and V. Peano, *Engineering Arbitrary Hamiltonians in Phase Space*, Phys. Rev. Lett. **132**, 023602 (2024).

- [55] A. Labay-Mora, R. Zambrini, and G. L. Giorgi, *Quantum memories for squeezed and coherent superpositions in a driven-dissipative nonlinear oscillator*, Phys. Rev. A **109**, 032407 (2024).
- [56] A. Yamaguchi, S. Masuda, Y. Matsuzaki, T. Yamaji, T. Satoh, A. Morioka, Y. Kawakami, Y. Igarashi, M. Shirane, and T. Yamamoto, *Spectroscopy of flux-driven Kerr parametric oscillators by reflection coefficient measurement*, New. J. Phys. **26**, 043019 (2024).
- [57] N. Lambert, E. Giguère, P. Menczel, B. Li, P. Hopf, G. Suárez, M. Gali, J. Lishman, R. Gadhvi, R. Agarwal, A. Galicia, N. Shammah, P. Nation, J. R. Johansson, S. Ahmed, S. Cross, A. Pitchford, and F. Nori, *QuTiP 5: The Quantum Toolbox in Python*, Phys. Rep. **1153**, 1 (2026).
- [58] A. Royer, *Wigner function as the expectation value of a parity operator*, Phys. Rev. A **15**, 449 (1977).
- [59] L. G. Lutterbach and L. Davidovich, *Method for Direct Measurement of the Wigner Function in Cavity QED and Ion Traps*, Phys. Rev. Lett. **78**, 2547 (1997).
- [60] S. Ahmed, C. Sánchez Muñoz, F. Nori, and A. F. Kockum, *Quantum State Tomography with Conditional Generative Adversarial Networks*, Phys. Rev. Lett. **127**, 140502 (2021).
- [61] S. Ahmed, C. Sánchez Muñoz, F. Nori, and A. F. Kockum, *Classification and reconstruction of optical quantum states with deep neural networks*, Phys. Rev. Research **3**, 033278 (2021).
- [62] Z. Wang, M. Pechal, E. A. Wollack, P. Arrangoiz-Arriola, M. Gao, N. R. Lee, and A. H. Safavi-Naeini, *Quantum dynamics of a few-photon parametric oscillator*, Phys. Rev. X **9**, 021049 (2019).
- [63] S. Kwon, S. Watabe, and J.-S. Tsai, *Autonomous quantum error correction in a four-photon Kerr parametric oscillator*, npj Quantum Inf. **8**, 40 (2022).
- [64] M. A. P. Reynoso, E. M. Signor, J. Khalouf-Rivera, A. D. Ribeiro, F. Pérez-Bernal, and L. F. Santos, *Phase transitions, symmetries, and tunneling in Kerr parametric oscillators*, Phys. Rev. A **112**, 032415 (2025).
- [65] Q. Su, R. G. Cortiñas, J. Venkatraman, and S. Puri, *Unraveling the switching dynamics in a quantum double-well potential*, Phys. Rev. A **112**, 042202 (2025).
- [66] X. You, J. A. Sauls, and J. Koch, *Circuit quantization in the presence of time-dependent external flux*, Phys. Rev. B **99**, 174512 (2019).
- [67] W. Wyss, *Two Non-Commutative Binomial Theorems*, Preprint at <https://doi.org/10.48550/arXiv.1707.03861> (2017).